Robust Estimation of Multiple Inlier Structures

Xiang Yang and Peter Meer

Abstract—In this paper we present a method to robustly estimate multiple inlier structures with different scales in the presence of noise. The estimation is done iteratively with the objective function transformed into a higher dimensional linear space by carrier vectors. An initial set consisting of a small number of points that has the minimum sum of Mahalanobis distances is detected from the trials based on elemental subsets. The region of interest is defined by applying an expansion criteria to an increasing sequence of sets of points which begins with the initial set and increases until the set cannot expand. The largest expansion in this region gives the scale estimate. The original mean shift is applied to all remaining input points to re-estimate the structure. After all data are processed, the segmented structures are sorted by strengths with the strongest inlier structures at the front. Several synthetic and real examples are presented to illustrate every aspect of the algorithm. This method is easy to implement and its limitations of robustness are clearly stated.

Index Terms—scale estimate, structure segmentation, strength based classification, heteroscedasticity in computer vision.

arXiv:1609.06371v2 [cs.CV] 23 Sep 2016

1 Introduction

In computer vision, the objective functions of inlier structures can be either linear, like the estimation of planes, or nonlinear, such as to find the homography between two images. The function can be satisfied by multiple inlier structures, and each structure can be corrupted by noise independently, resulting in different scales. Since all the other points are considered as outliers for a single inlier structure, when multiple structures exist, the input data have lower inlier ratios. A robust estimator detects every inlier structures from the input data, while removing the structureless outliers.

Elemental subsets are the building blocks of the robust regression. Each randomly chosen subset has the minimum number of points required to estimate the parameters in the objective function. The most used algorithm for robust fitting in the past 35 years is the RANdom SAmple Consensus (RANSAC) [8]. Similar types of methods also exist, like PROSAC, MLESAC, Lo-RANSAC, etc. Asides from the different ways to generate the random sampling, these methods also use probabilistic relations for the elimination of the outliers. In the paper [23] a review of these methods is given.

In [22] a universal framework for RANSAC, the USAC, was introduced. However, the USAC failed in the homography estimation when a wide angle existed between two images [16]. In [15] RANSAC was combined with the projection based M-estimator [3], to detect primitives such as planes, spheres, cylinders, etc., in 3D range data. The Darboux frame of orthogonal triplets was used for datasets with thousands of input points. The data were acquired by 3D scanner, and the method was tested with relatively small noise. Whether it can work on noisier inputs containing randomly distributed outliers was not verified.

A major drawback of RANSAC is that the user has to give a suitable value as the inlier scale. In real images, for homography and fundamental matrix, the inlier noise is usually less than 2-3 pixels and RANSAC is successful. When the input images are scaled and cropped before estimation, the value given to the RANSAC may no longer be valid for a correct result. Problems also appear if multiple inlier structures with different noise level exist, or if the inlier noise varies in a sequence of images.

In [29], several techniques were described which do not require the scale value from the user. Most of the methods still have one or more parameters related to the scale estimation which are given beforehand. The paper also proposed a new method to estimate the scale based on the k-th ordered absolute residual. The value of k was selected as 10% of all the input data in the experiments.

Energy-based minimization approach was used to optimize the quality of the entire solution in the Propose Expand and Re-estimate Labels (PEARL) method [13]. This algorithm started with RANSAC, followed by alternative steps of expansion (inlier classification) and re-estimation, while minimizing the energy of the errors. The regularization was performed by Markov Random Field (MRF) with the input points represented by Delaunay triangulation. The method converged to a local optimum with a small number of inlier structures. A synthetic example in figure 11 showed that PEARL can handle different levels of Gaussian noise in multiple 2D line models; however, the difference in the noise levels in real images were not mentioned. The amount of outliers were relatively small in all the estimations.

The Random Cluster Model SAmpler (RCMSA) in [21] was similar to [13], but simulated annealing was used to minimize the overall energy function. Small clusters were discarded based on a function of the average fitting error. In the comparison of different algorithms, RCMSA performed better than PEARL. The number of outliers were always smaller than the number of inliers. The scalar segmentation error may not fully indicate the correctness of the results, since for the same segmentation error value more outliers can be tolerated with a larger number of inliers.

The method in [27] used the higher than minimal subset

• *X. Yang (Dept. of Mechanical and Aerospace Engineering), P. Meer (Dept. of Electrical and Computer Engineering), Rutgers University, NJ 08854, USA. E-mail: {xiang.yang@, meer@cronos}.rutgers.edu*

approach by randomly selecting $p+2$ points, where p was the size of the elemental subset, then computing the least k-th order statistics and iteratively improving it. The significance of the additional two points in the sample was justified empirically, for the 2D line fitting it was 100% more than the elemental subset, but only 25% more for the fundamental matrix. The parameter k varied in the experiments, for 2D line fitting it was 10% of the total number of points, and between 20 to 40 for homography detections. The number of inlier structures had to be provided for better results, otherwise the sparse subspace clustering [7] gave smaller errors for the 3D motion segmentation.

The 2D homography estimation in [16] had a different approach. A very dense sampling of the grid was combined with probabilistic reasoning to obtain the inlier rate estimate. This sampling procedure was extensive and even though a large quantity of outliers can be present, only one inlier structure can be recovered.

The generalized projection-based M-estimator (gpbM) [18] used elemental subsets for robust estimation. Three independent steps existed in each iteration: scale estimation, mean shift based recovery of the structure and inlier/outlier dichotomy. The first step estimated the scale from the highest weighted value, which was the cumulative distribution function of a segment weighted by its size. This implementation was targeted to make a structure containing more points easier to be detected first. The factor used as weight was important in order to obtain the correct scale estimate. In figure 3c the correct scale was not detected, while in figure 3d the maximum weighted density value is correct. This strategy, however, may not work all the time.

The new algorithm presented in the following sections will have several major differences from the gpbM.

- Instead of the scale estimation in gpbM with all the remaining input data involved, the new scale estimation begins with a small set of points from one structure.
- The gpbM used an adaptive form of mean shift to refine the scale estimate result, while the original form of mean shift [6] is applied in the new method.
- The gpbM stopped when the estimation was weaker than a given threshold. In the new method, all input points are segmented, and the inlier structures are returned as the strongest ones.

The only parameter to be specified by user is the number of trials for random sampling.

The linearized objective functions are presented in Section 2. The algorithm of the new robust estimator is detailed in Section 3. Examples including the estimation of 2D lines, 2D ellipses, 3D cylinders, fundamental matrices and homographies are given in Section 4. Finally, in Section 5 we discuss some open problems.

2 From a Nonlinear to a Linear Space

In Section 2.1, the nonlinear objective function of the inputs is transformed into a linear function of the carrier vectors. The first order approximation of the covariance matrix of these carriers is also computed. Section 2.2 explains how the largest Mahalanobis distance of each input point is taken into account when multiple carrier vectors are derived.

2.1 Carrier vectors

The nonlinear objective functions in computer vision can be transformed into linear relations in higher dimensions. These linear relations contain terms formed by the measurements in the inputs and their pairwise products, which are called *carriers*, and each relation gives a carrier vector. For linear objective functions, such as plane fitting, the input variables and the carrier vector are identical.

For example, in the estimation of fundamental matrix the input data $\mathbf{y}$ are the point correspondences from two images $[x \;\; y \;\; x' \;\; y']^\top \in \mathbb{R}^4$, with $l = 4$ dimensions. The objective function with noisy image coordinates is

$$[x' \;\; y' \;\; 1] \; \mathbf{F} \; [x \;\; y \;\; 1]^\top \simeq 0 \tag{1}$$

which gives a carrier vector $\mathbf{x} \in \mathbb{R}^8$ containing $m = 8$ carriers

$$\mathbf{x} = [x \;\; y \;\; x' \;\; y' \;\; xx' \;\; xy' \;\; yx' \;\; yy']^\top . \tag{2}$$

The linearized function of the carriers is

$$\mathbf{x}_i^\top \boldsymbol{\theta} - \alpha \simeq 0 \quad i = 1, \ldots, n_{in} \tag{3}$$

where n_{in} denotes the number of inliers. Vector $\boldsymbol{\theta} \in \mathbb{R}^8$ and scalar intercept α derived from the 3×3 matrix $\mathbf{F}$ are to be estimated. The constraint $\boldsymbol{\theta}^\top \boldsymbol{\theta} = 1$ eliminates the multiplicative ambiguity in (3). The same constraint was also used in [19] to have the estimation results in gpbM further refined on the Grassmann manifold. The same improvement could be applied at the end of the new algorithm, but will be not discussed in this paper.

In the general case, several linear equations can be derived from a single input $\mathbf{y}_i$

$$\mathbf{x}_i^{[c]\top} \boldsymbol{\theta} - \alpha \simeq 0 \quad c = 1, \ldots, \zeta \quad i = 1, \ldots, n_{in} \tag{4}$$

corresponding to ζ different carrier vectors $\mathbf{x}^{[c]}$. For example, the estimation of homography has $\zeta = 2$ carrier vectors derived from x and y image coordinates.

The Jacobian matrix is required for the first order approximation of the covariance of carrier vector. From each carrier vector $\mathbf{x}^{[c]}$, an $m \times l$ Jacobian matrix $\mathbf{J}_{\mathbf{x}^{[c]}|\mathbf{y}}$ is derived. Each column of the Jacobian matrix contains the derivatives of the m carriers in $\mathbf{x}^{[c]}$ with respect to one measurement from $\mathbf{y}$. The Jacobian matrices derived from linear objective functions are not input dependent, while those derived from nonlinear objective functions rely on the specific input point. The carrier vectors are *heteroscedastic* for nonlinear objective functions. For example, the transpose of the 8×4 Jacobian matrix of the fundamental matrix

$$\mathbf{J}_{\mathbf{x}_i|\mathbf{y}_i}^\top = \begin{bmatrix} 1 & 0 & 0 & 0 & x_i' & y_i' & 0 & 0 \\ 0 & 1 & 0 & 0 & 0 & 0 & x_i' & y_i' \\ 0 & 0 & 1 & 0 & x_i & 0 & y_i & 0 \\ 0 & 0 & 0 & 1 & 0 & x_i & 0 & y_i \end{bmatrix} \tag{5}$$

depends on $\mathbf{y}_i$.

The $l \times l$ covariance matrix of the measurements $\sigma^2 \mathbf{C}_\mathbf{y}$ with $\det \mathbf{C}_\mathbf{y} = 1$, has to be provided before estimation. This is a

chicken-egg problem, since the input points have not yet been classified into inliers and outliers. A reasonable assumption is to set $\mathbf{C_y}$ as the identity matrix $\mathbf{I_y}$, if no additional information is given. The input data are considered as independent and identically distributed, and contain *homoscedastic* measurements with the same covariance.

The covariance of the carrier vector $\sigma^2\mathbf{C}_i^{[c]}$ is computed from

$$\sigma^2\mathbf{C}_i^{[c]} = \sigma^2\mathbf{J}_{\mathbf{x}_i^{[c]}|\mathbf{y}_i}\ \mathbf{C_y}\ \mathbf{J}^{\top}_{\mathbf{x}_i^{[c]}|\mathbf{y}_i} \tag{6}$$

where the dimensions of $\mathbf{C}_i^{[c]}$ is $m \times m$. The scale σ of the structure is unknown and to be estimated.

2.2 Computation of the Mahalanobis distances

The elemental subset needs $m_e = \lceil \frac{m}{\zeta} \rceil$ input points to uniquely define $\boldsymbol{\theta}$ and α in the linear space. For example, the homography $(m = 8,\ \zeta = 2)$ requires four point pairs, and eight pairs are necessary for the fundamental matrix $(m = 8,\ \zeta = 1)$ if the 8-point algorithm is used. The input data should be normalized [10, Section 4.4], and have the obtained structures mapped back onto the original space.

For each $\boldsymbol{\theta}$, every carrier vector is projected to a scalar value $z_i^{[c]} = \mathbf{x}_i^{[c]\top}\boldsymbol{\theta},\ c = 1, \ldots, \zeta$. The average projection of the m vectors from an elemental subset is α. The variance of $z_i^{[c]}$ is $\sigma^2 H_i^{[c]} = \sigma^2\boldsymbol{\theta}^{\top}\mathbf{C}_i^{[c]}\boldsymbol{\theta}$.

The Mahalanobis distance, indicating how far is a projection $z_i^{[c]}$ from α, is computed from

$$\begin{aligned} d_i^{[c]} &= \sqrt{\left(\mathbf{x}_i^{[c]\top}\boldsymbol{\theta} - \alpha\right)^{\top}\left(H_i^{[c]}\right)^{-1}\left(\mathbf{x}_i^{[c]\top}\boldsymbol{\theta} - \alpha\right)} \\ &= \frac{|\mathbf{x}_i^{[c]\top}\boldsymbol{\theta} - \alpha|}{\sqrt{\boldsymbol{\theta}^{\top}\mathbf{C}_i^{[c]}\boldsymbol{\theta}}} \qquad c = 1, \ldots, \zeta. \end{aligned} \tag{7}$$

Each input point $\mathbf{y}_i$ gives a ζ-dimensional Mahalanobis distance vector

$$\mathbf{d}_i = \left[\begin{array}{ccc} d_i^{[1]} & \ldots & d_i^{[\zeta]} \end{array}\right]^{\top} \qquad i = 1, \ldots, n. \tag{8}$$

The worst-case scenario is taken to retain the largest Mahalanobis distance $d_i^{[\tilde{c}_i]}$ from all the ζ values

$$\tilde{c}_i = \underset{c=1,\ldots,\zeta}{\arg\max}\ d_i^{[c]}. \tag{9}$$

For different $\boldsymbol{\theta}$-s, the same input point may have its largest distance computed from different carriers.

The symbols related to the largest Mahalanobis distance are: $\tilde{d}_i$, the largest Mahalanobis distance for input $\mathbf{y}_i$; $\tilde{\mathbf{x}}_i$, the $m \times 1$ carrier vector; $\tilde{z}_i$, the scalar projection of $\tilde{\mathbf{x}}_i$; $\widetilde{\mathbf{C}}_i$, the $m \times m$ covariance matrix of $\tilde{\mathbf{x}}_i$; $\widetilde{H}_i$, the variance of $\tilde{z}_i$; $\hat{\sigma}$, the scale multiplying $\widetilde{\mathbf{C}}_i$ and $\widetilde{H}_i$, is to be estimated.

3 Estimation of Multiple Structures

The new algorithm is detailed in this section. The scale $\hat{\sigma}$ for a structure is estimated in Section 3.1 by an expansion criteria. The estimated scale is used in the mean shift to re-estimate the structure in Section 3.2. The iterative process continues until not enough input points remain for a further estimation. In Section 3.3 all the estimated structures are ordered by strengths with the strongest inlier structures returned first. The limitations of the method are explained in Section 3.4.

3.1 Scale estimation for a structure

Assume that n input points remain in the current iteration. The estimation process starts with M randomly generated elemental subsets, each giving a $\boldsymbol{\theta}$ and an α.

For every point $\mathbf{y}_i$, compute the largest Mahalanobis distance $\tilde{d}_i$

$$\tilde{d}_i = \frac{|\tilde{\mathbf{x}}_i^{\top}\boldsymbol{\theta} - \alpha|}{\sqrt{\boldsymbol{\theta}^{\top}\widetilde{\mathbf{C}}_i\boldsymbol{\theta}}} \geq 0 \qquad i = 1, \ldots, n. \tag{10}$$

Sort the n-distances in ascending order, denoted $\tilde{d}_{[i]}$. We get M sorted sequences from all the trials .

Let $n_\epsilon \ll n$ represent a small amount of points

$$n_\epsilon = \frac{\epsilon\, n}{100} \qquad 0 < \epsilon \ll 100 \tag{11}$$

where ϵ defines the size of n_ϵ in percentage of the remaining inputs.

Among all M trials, find the sequence that gives the *minimum sum* of Mahalanobis distances from the first n_ϵ points

$$\min_M \sum_{i=1}^{n_\epsilon} \tilde{d}_{[i]}. \tag{12}$$

The sequence retained is denoted by $\tilde{d}_{[i]_M},\ i = 1, \ldots, n$, and the first n_ϵ points are collected as the initial set.

If M is sufficiently large and the inlier structures still exist to be detected, these n_ϵ points have a high probability to be selected from a single inlier structure, since it is more dense than the outliers. The size of n_ϵ is assigned heuristically, as neither information on the number of structures, nor the inlier amounts for each structure is known beforehand.

Two rules should be considered for the ratio $\epsilon\%$. First, n_ϵ should be smaller than the size of any inlier structure to be estimated. Therefore, a small ratio is preferred to detect potential structures. In the following sections, all our experiments start with $\epsilon\% = 5\%$. The second rule is to have the size of n_ϵ at least five times the number of points in the elemental subset, as suggested in [10, page 182]. This condition reduces unstable results when relatively few input points are provided.

The sorted sequence $\tilde{d}_{[i]_M}$ contains more inlier points besides those in the initial set. To recover the scale $\hat{\sigma}$, as many as possible points belonging to the same structure have to be classified together. The following example explains the expansion criteria used for scale estimation.

In Fig.1a two ellipses are shown, each of them has $n_{in} = 200$ inlier points. They are corrupted by different Gaussian noise with standard deviation $\sigma_g = 5$ and 10 respectively. Another $n_{out} = 200$ outliers are randomly placed in the 700×700 image. With $M = 2000$ and $\epsilon\% = 5\%$ $(n_\epsilon = 30)$ we obtain the initial set in Fig.1b. The distances in $\tilde{d}_{[i]_M}$ for the first 400 points are shown in Fig.1c.

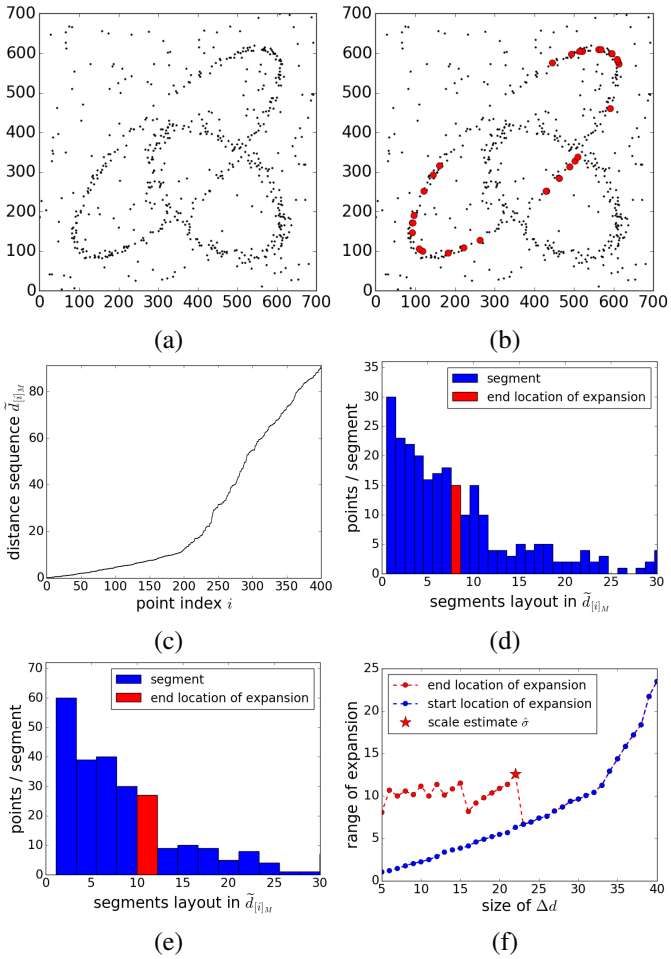

Fig. 1. Scale estimation. (a) Input data. (b) Initial set for an iteration. (c) The first 400 points in the sequence $\tilde{d}_{[i]_M}$. (d) Histogram of point amounts with segment size $\Delta d = \tilde{d}_{[5\%]_M}$. (e) Histogram of point amounts with segment size $\Delta d = \tilde{d}_{[10\%]_M}$. (f) Expansion criteria applied to increasing sets.

Divide the $\tilde{d}_{[i]_M}$ sequence into multiple segments of equal length Δd. Start with the largest distance from the initial set $\Delta d = \tilde{d}_{[\epsilon\%]_M}$, the first segment $k = 1$ contains n_ϵ points (Fig.1d). Let n_k denote the total number of points within the k segments, $k = 1, 2, \ldots$, the expansion process verifies the following condition for each k

$$\frac{n_{k+1} - n_k}{n_k / k} \leq 0.5 \tag{13}$$

where the numerator is the number of points in the $(k+1)$-th segment and the denominator is the average point numbers inside the k segments. When the point density drops below half of the average in the previous segments, the boundary to separate the inliers from the outliers is found. The value of this scale estimate is $k_t \Delta d$.

The condition (13) is easy to implement compared to the method proposed in [16]. However, due to the randomness of the input data, a single estimation of the scale may not be good enough. If the size of initial set is too small compared with the true structure, the scale estimate can also be too small to fully recover the complete structure in the mean shift.

In Fig.1d the expansion starting with $\Delta d = \tilde{d}_{[5\%]_M}$ stops at $k_t = 8$, giving $\hat{\sigma} = 8.06$ (red bar). This is a relatively small estimate since a scale larger than 10 is expected when $\sigma_g = 5$. In Fig.1e a larger $\Delta d = \tilde{d}_{[10\%]_M}$ is applied, and the expansion stops at $k_t = 5$ giving $\hat{\sigma} = 11.10$. This shows that various estimates can be generated from different layouts of segments, which is similar to the smoothing process when different smooth kernel sizes are used.

In Fig.1f the expansion process is applied to an increasing sequence of sets. The Δd starts from $\tilde{d}_{[\epsilon\%]_M}$ and increases by 1% for each new sampling. The blue points in the figure indicate the length of Δd in percentage of points used as the segment size. Every expansion process is performed separately, and stops at the corresponding red point when condition (13) is met. The length of Δd continues to increase until it reaches the bound where the sets can no longer expand, as it is 23% in Fig.1f.

The scale estimate is found from this *region of interest* where the sets of points can expand. In Fig.1f it ranges from 5% to 22%. The expansion may not always start from $\epsilon\%$, as the Δd increases the region of interest starts only where the expansion process begins.

The largest estimate from the region of interest gives the scale $\hat{\sigma}$

$$\hat{\sigma} = \max k_t \Delta d \qquad \text{in region of interest} \tag{14}$$

which is to find the farthest expansion inside the region of interest as $\hat{\sigma}$. In Fig.1f the scale estimate is $\hat{\sigma} = 12.54$. From the sequence $\tilde{d}_{[i]_M}$, collect all the points within the scale estimate for the next step.

If the scale estimator locates an outlier structure, $\hat{\sigma}$ in general is much larger and the structure has weaker strength than inlier structures, as discussed in Section 3.3.

3.2 Mean shift based structure recovery

From the points collected in the first step, another $N \ll M$ elemental subsets are generated. Most points in this set come from the same structure thus $N = M/10$ is enough.

For each trial all the input points are projected by $\boldsymbol{\theta}$ to a one-dimensional space $\tilde{z}_i = \tilde{\mathbf{x}}_i^\top \boldsymbol{\theta}$, $i = 1, \ldots, n$. The mean shift [6] moves the z from $z = \alpha$ to the *closest mode*

$$\begin{aligned} \left[\widehat{\boldsymbol{\theta}}, \widehat{\alpha}\right] &= \arg\max_{\boldsymbol{\theta}, \alpha} \frac{1}{n\hat{\sigma}} \sum_{i=1}^{n} \kappa\left((z - \tilde{z}_i)^\top \widetilde{B}_i^{-1} (z - \tilde{z}_i) \right) \\ &= \frac{1}{n\hat{\sigma}} \arg\max_{\boldsymbol{\theta}} \left(\arg\max_{z} f_{\boldsymbol{\theta}}(z) \right). \end{aligned} \tag{15}$$

The variance $\tilde{B}_i$ is computed from

$$\begin{aligned} \widetilde{B}_i &= \hat{\sigma}^2 \widetilde{H}_i = \hat{\sigma}^2 \boldsymbol{\theta}^\top \tilde{\mathbf{C}}_i \boldsymbol{\theta} \\ &= \hat{\sigma}^2 \boldsymbol{\theta}^\top \mathbf{J}_{\tilde{\mathbf{x}}_i | \mathbf{y}_i} \mathbf{J}_{\tilde{\mathbf{x}}_i | \mathbf{y}_i}^\top \boldsymbol{\theta} \end{aligned} \tag{16}$$

with $\mathbf{C}_\mathbf{y} = \mathbf{I}_\mathbf{y}$ in general.

The function $\kappa(u)$ is the profile of a radial-symmetric kernel

$K(u^2)$ defined only for $u \geq 0$. For the Epanechnikov kernel

$$\kappa(u) = \begin{cases} 1-u & (z-\widetilde{z}_i)^\top \widetilde{B}_i^{-1}(z-\widetilde{z}_i) \leq 1 \\ 0 & (z-\widetilde{z}_i)^\top \widetilde{B}_i^{-1}(z-\widetilde{z}_i) > 1. \end{cases} \tag{17}$$

Let $g(u) = -\kappa'(u)$ and for the Epanechnikov kernel, $g(u) = 1$ when $0 \leq u \leq 1$ and 0 if $u > 1$. All the points inside the window contribute equally in the mean shift. The convergence to the closest mode is obtained by assigning zero to the gradient of (15) in each iteration. The z_{new} is updated from the current value $z = z_{old}$ by

$$z_{new} = \left[\sum_{i=1}^{n} g\left(u\right)\right]^{-1}\left[\sum_{i=1}^{n} g\left(u\right)\widetilde{z}_i\right]. \tag{18}$$

Many of the n input points have their projections more distant from z_{old} than $\pm\widetilde{B}_i$ and their weights are zeros.

The highest mode among all N trials gives the estimate $\hat{z} = \hat{\alpha}$. The vector $\hat{\boldsymbol{\theta}}$ is obtained from the same elemental subset which gives the highest mode. All the input points that can converge into the $\pm\hat{\sigma}$ region around $\hat{\alpha}$ are classified as inliers, resulting in n_{in} points. The total least squares (TLS) estimate for the structure is computed and $\hat{\boldsymbol{\theta}}^{tls}$, $\hat{\alpha}^{tls}$ and $\hat{\sigma}^{tls}$ are obtained.

3.3 Strength based classification

After the mean shift step, the n_{in} points are removed from the inputs before the next iteration. If the remaining data are not enough for another initial set, the algorithm terminates and all the recovered structures are sorted by their strengths in descending order. The *strength of a structure* is defined as

$$s = \frac{n_{in}}{\hat{\sigma}^{tls}}. \tag{19}$$

which can also be seen as the density in the linear space. The value n_{in} is more general than just the number of points in an inlier structure, since it also represents the point amount when an outlier structure is returned.

The algorithm detects structures with stronger strengths first, and segments all the input data into different structures. The inlier structures are more dense and have smaller scales in general, while the outlier structures have weaker strengths. In practice the users can retain the preferred number of structures based on the sorted result, or apply a threshold for the scale $\hat{\sigma}^{tls}$. Experiments on the strength based classification will be presented in Section 4.

3.4 Limitations

Every robust estimator has its limitations. For the new algorithm, one of the limitations comes from the interactions between inliers and outliers in the linear space. We can use a simple example to illustrate this.

In a 700×700 image, a circle consists of $n_{in} = 200$ inliers is corrupted by Gaussian noise with $\sigma_g = 10$, together with $n_{out} = 1500$ outliers. The first circle has a radius of 50 (Fig.2a), and the other one has a radius of 200 (Fig.2c). Both these figures give the correct scale estimates, $\hat{\sigma}_{50} = 23.65$ and $\hat{\sigma}_{200} = 23.58$.

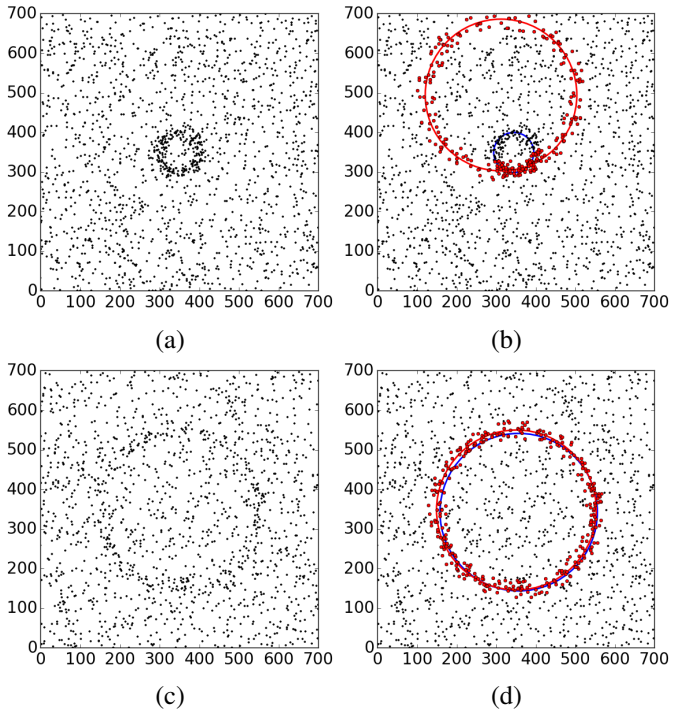

Fig. 2. The inlier/outlier interaction. (a) Input data of a circle with radius 50. (b) Incorrect final result obtained from a correct scale estimate. (c) Input data of a circle with radius 200. (d) Good final result obtained from a correct scale estimate.

However, after the mean shift step an incorrect final circle is obtained in Fig.2b. A total of 261 points are collected as inliers on the red circle, where 84 points are from true inliers and 177 points from the outliers. In the true inlier structure, around 196 points should exist inside the scale $\hat{\sigma}_{50} = 23.65$, based on the Gaussian distribution. The number of outliers in the same location can be roughly estimated as

$$(2\pi\, 50)(2 * 23.65)\frac{1500}{700 \times 700} = 45 \text{ points.}$$

thus about 241 points can be covered in the correct circle, while the 261 points from the incorrect circle form a larger amount. Therefore, the mean shift converges to another mode due to the heavy noise from outliers.

Although the circle in Fig.2c appears much weaker, after 100 tests with randomly generated data (inlier/outlier), it returns more stable estimations than the smaller circle in Fig.2a. In a result shown in Fig.2d, 346 points are classified as inliers, where 190 points are from true inliers and 156 points from the outliers. The mean shift has a much lower probability to converge to another, incorrect, mode and this inlier structure resists more outliers.

The limitation also exists in RANSAC when many outliers are present. An incorrect estimation could be returned even if the correct scale is given by the user. This is different than failing due to not explicitly considering the underlying task [11]. The methods proposed in [21] and [27] will also return incorrect results if too many outliers exist.

A robust estimator was proposed by combining an extended

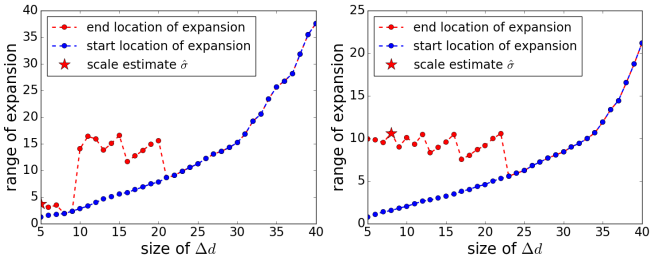

Fig. 3. Limitation of scale estimation. (a) Unstable estimate obtained from a small number of inliers ($n_{in} = 200, n_{out} = 400$). (b) More robust estimate obtained from a larger number of inliers ($n_{in} = 400, n_{out} = 400$).

Kalman filter with a structure from motion algorithm in [28], to track objects in an image sequence. In figure 5 the real data contained more than 60% outliers with small inlier noise. In [20], the homography estimation in figure 6 has more than 90% of the points as outliers. Almost 10000 iterations were required using a contrario type outlier elimination, to return the correct inliers. Since the results from repetitive tests were not shown in these papers, the stability of the methods cannot be verified.

The noise level of the inliers also affects the number of outliers that can be tolerated. With the same number of inliers, structures with lesser inlier noise can be estimated more robustly since a smaller scale estimate results in a stronger strength. Once the amount of outliers reaches the limit, the weakest inlier structure cannot be recovered most of the time. Preprocessing is required to reduce the number of outliers in order to have better performance.

Another limitation appears when the scale is not estimated properly. If a value much smaller than the true scale is returned, it may not fully converge the majority of the inlier points into one structure. Similarly, the same problem appears if the initial set is not closely aligned with a true inlier structure because of the outlier noise.

In Fig.3a, the expansion process is applied to the same example as in Fig.1, but with $n_{out} = 400$. The expansion stops soon and the algorithm locates the region of interest between $5\%-7\%$, and gives a small scale. After applying the expansion criteria many times, the range of expansion from different sets are not stable. In Fig.3b the number of inliers is raised to 400. The scale becomes a more stable estimate with the region of interest located between $5\% - 22\%$. Preprocessing is helpful here too to reduce the number of outlier points.

When the scale estimator reaches its limitation, an inlier structure may appear split and post processing is required to merge them. The user can easily locate them by their strengths since most these splitted structures are still stronger compared with the outliers. The similarity of two structures should be compared in the input space where measurements are obtained, as the derived carriers in the linear space do not represent the nonlinearities of the inputs explicitly.

For two inlier structures with linear objective function, the merge can be implemented based on the orientation of each structure and the distance between them. For two ellipses, the geometric tools to determine the overlap area can be used [12]. The measurements of fundamental matrices and the homographies are in the projective space instead of euclidean. Fig.12 in Section 4 shows multiple orthogonal planes in the 3D euclidean space, however their corresponding 2D homographies are very similar due to the small motion. Therefore the merge condition on the 2D data has to be carefully applied to avoid any unnecessary merge. If the reconstructed 3D scene can be provided from auto-calibration [10, Chapter 19], the 3D information can be applied for a merge.

3.5 Review of the algorithm

The new algorithm is summarized below.

Robust estimation of multiple inlier structures

Input: $\mathbf{y}_i$, $i = 1, \ldots, n$ data points that contain an unknown number of inlier structures with their scales unspecified, along with outliers. The covariance matrices for $\mathbf{y}_i$ are $\mathbf{C}_\mathbf{y} = \mathbf{I}_\mathbf{y}$ if not provided explicitly.

Output: The sorted structures with inliers coming out first.

- Compute the carriers $\mathbf{x}_i^{[c]}$, $c = 1, \ldots, \zeta$, and the Jacobians $\mathbf{J}_{\mathbf{x}_i^{[c]}|\mathbf{y}_i}$, for each input $\mathbf{y}_i$, $i = 1, \ldots, n$.

$\odot$ Generate M random trials based on elemental subsets.

- For each elemental subset find $\boldsymbol{\theta}$ and α.
- Compute the Mahalanobis distances from α for all carriers $\mathbf{x}_i^{[c]}$, $c = 1, \ldots, \zeta$. Keep the largest distance $\tilde{d}_i$ for each point.
- Sort the Mahalanobis distances in ascending order.
- Among all M trials, find the sequence $\tilde{d}_{[i]_M}$ with the minimum sum of distances for $\epsilon\%$ of the input points still in processing.

- Apply the expansion criteria to an increasing sequence of sets and determine the region of interest for a structure.
- In the region of interest find the largest estimate as $\hat{\sigma}$ and collect all points.
- Generate $N \ll M$ random trials from these points.
  - Apply the mean shift to all still existing points, to find the closest mode from α.
  - Find $\hat{\alpha}$ at the maximum mode among all N trials, and $\hat{\boldsymbol{\theta}}$ from the same elemental subset.
  - The recovered structure contains n_{in} points which converged to $\pm\hat{\sigma}$ from $\hat{\alpha}$.
- Compute the TLS solution for the structure and remove the n_{in} points from the inputs.
- Go back to $\odot$ and start another iteration.
- If not enough input points remain, sort all structures by their strengths and return the result.

4 Experiments

Several synthetic and real examples are presented in this section. In most cases a single carrier exists, $\zeta = 1$, except

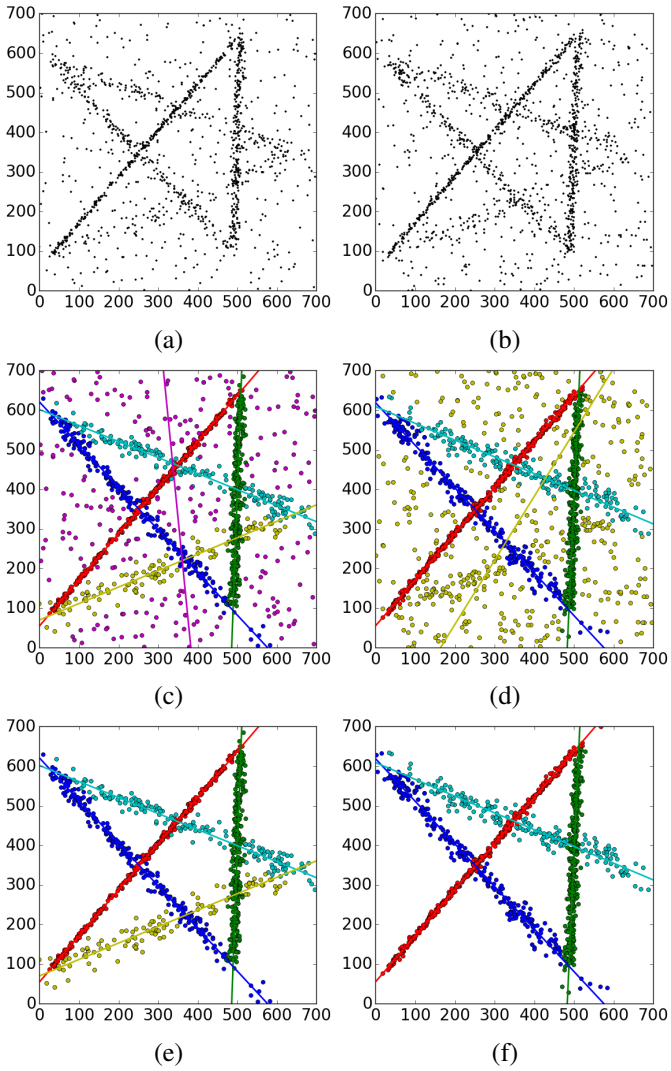

Fig. 4. Synthetic 2D line estimations. (a) Case 1: five lines with 350 outliers. (b) Case 2: five lines with 500 outliers. (c) Recovered six structures, case 1. (d) Recovered five structures, case 2. (e) Five strongest structures, case 1. (f) Four strongest structures, case 2.

for the homography estimation which has two carriers, $\zeta = 2$. The Epanechnikov kernel is used in the mean shift.

The input data for synthetic problems are generated randomly in each test. Gaussian noise is added to each inlier structure. The standard deviation σ_g is specified but not used in the processing. The values of scale and inlier amount are returned as the output of the algorithm.

4.1 2D Line

In the first synthetic example we estimate *multiple 2D lines*. The noisy objective function is

$$\theta_1 x_i + \theta_2 y_i - \alpha \simeq 0 \qquad i = 1, \ldots, n_{in}. \tag{20}$$

The input variable $\mathbf{y} = [x \; y]^\top$ is identical with the carrier vector $\mathbf{x}$. This case is homoscedastic.

Five lines are placed in a 700×700 plane (Fig.4a) and corrupted with different two-dimensional Gaussian noise. They have $n_{in} = 300, 250, 200, 150, 100$ inlier points, and $\sigma_g = 3, 6, 9, 12, 15$, respectively. Another 350 unstructured outliers are uniformly distributed in the image. The amount of points inside each inlier structure is small compared with the entire data.

With $M = 1000$, a test result is shown in Fig.4c. The algorithm recovers six structures

	red	*green*	*blue*	*cyan*	*yellow*	*purple*
scale :	9.6	18.7	28.1	37.1	44.2	370.8
inliers :	321	282	240	161	106	240
strength :	33.4	15.1	8.5	4.3	2.4	0.6.

When the user retains only the first five structures, Fig.4e is obtained. The sixth structure formed with outliers has a lower strength than the inlier structures.

When the randomly generated inputs are tested 100 times, in 94 times the algorithm gives correct results for all the five inlier structures as the strongest ones. In the other six tests, the weakest line is not segmented properly, while the first four lines are still correct. The average result of the scale estimates and the classified inliers along with their standard deviations are

scale :	10.48	19.94	29.36	36.86	38.17
	(1.17)	(2.44)	(5.30)	(10.40)	(18.29)
inliers :	335.9	285.8	240.8	155.6	93.4
	(8.2)	(9.5)	(21.3)	(27.0)	(28.4).

This result considers only the correct structure estimations, thus the fifth structure is averaged from 94 tests. In general, the estimated scale covers a $3\sigma_g$ area of an inlier structure. The number of true inliers is less than the classified inliers due to the presence of outliers in the same area.

As the outlier amount increases, the weakest structure will gradually blend into the background, and the expansion criteria can hardly separate inliers and outliers for this structure. In Fig.4b a case is shown where the outlier amount is raised to 500 instead of 350, and the number of inliers remain the same. In Fig.4d five structures are returned

	red	*green*	*blue*	*cyan*	*yellow*
scale :	12.0	18.6	33.8	41.5	483.6
inliers :	351	304	256	182	407
strength :	29.3	16.4	7.6	4.4	0.8.

The last structure is mixed with the outliers and is not estimated correctly. The first four inlier structures are still retained based on the strength (Fig.4f). In 100 tests the weakest line is detected 64 times, the fourth structure in 98 times, while the three strongest structures are estimated correctly in all trials.

In Fig.5a and Fig.5b two real images are shown. From Canny edge detection, 8310 and 8072 points are obtained in Fig.5c and Fig.5d. With $M = 1000$, the strongest results are superimposed over the original images in Fig.5e and Fig.5f.

4.2 2D Ellipse

In the next experiment we estimate *multiple 2D ellipses*. The noisy objective function is

$$(\mathbf{y}_i - \mathbf{y}_c)^\top \mathbf{Q} (\mathbf{y}_i - \mathbf{y}_c) - 1 \simeq 0 \qquad i = 1, \ldots, n_{in} \tag{21}$$

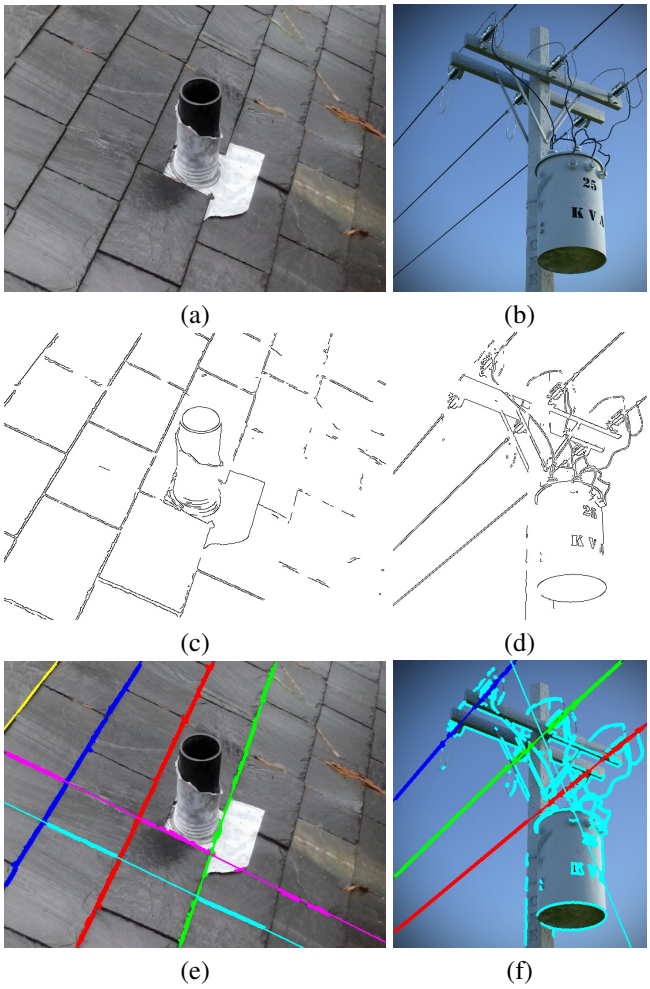

Fig. 5. 2D lines in real images. (a) Input image, *roof*. (b) Input image, *pole*. (c) *Roof*: Canny edges, 8310 points. (d) *Pole*: Canny edges, 8072 points. (e) *Roof*: six strongest structures. (f) *Pole*: three strongest structures and one outlier structure.

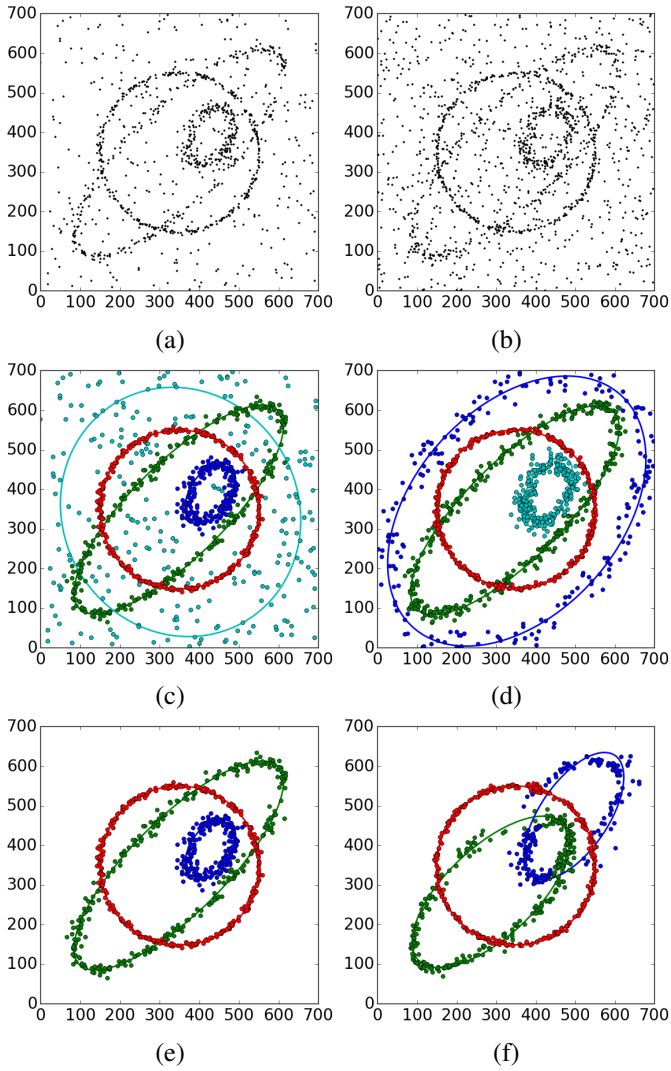

Fig. 6. Synthetic 2D ellipse estimations. (a) Case 1: three ellipses and 350 outliers. (b) Case 2: three ellipses and 800 outliers. (c) Recovered four structures, case 1. (d) Recovered first four structures, case 2. (e) Three strongest structures, case 1. (f) Interaction between two ellipses, case 2.

where $\mathbf{Q}$ is a symmetric 2×2 positive definite matrix and $\mathbf{y}_c$ is the position of the ellipse center. Given the input variable $\mathbf{y} = [x\ y]^\top$, the carrier is derived as $\mathbf{x} = [x\ y\ x^2\ xy\ y^2]$. The condition $4\theta_3\theta_5 - \theta_4^2 > 0$ also has to be satisfied in order to represent an ellipse. In practice, we also enforce the constraint that the major axis cannot be 10 times longer than the minor axis, to avoid classifying line segment as a part of a very flat ellipse.

The transpose of the 5×2 Jacobian matrix is

$$\mathbf{J}_{\mathbf{x}|\mathbf{y}}^\top = \begin{bmatrix} 1 & 0 & 2x & y & 0 \\ 0 & 1 & 0 & x & 2y \end{bmatrix}. \tag{22}$$

The ellipse fitting is a nonlinear estimation and is biased, especially for the part with large curvature. When the inputs are perturbed with zero mean Gaussian noise with standard deviation σ_g, the carrier vector $\mathbf{x}$ expressed as second order Taylor series is not zero mean compared with $\mathbf{x}_o$

$$\mathbf{E}(\mathbf{x} - \mathbf{x}_o) = [0 \quad 0 \quad \sigma_g^2 \quad 0 \quad \sigma_g^2]^\top \tag{23}$$

since the carrier contains x^2, y^2 terms. It is difficult to recover the ellipse structure even in the case where only inliers exist. A bias in the estimate can be clearly seen when only a part of the noisy ellipse is given in the input. Taking into account the second order statistics still cannot completely eliminate the bias. See the papers [14], [26] and the references inside for additional methods.

In Fig.6a three ellipses are placed with 350 outliers in the background. The inlier structures have $n_{in} = 300, 250, 200$ and $\sigma_g = 3, 6, 9$. The smallest ellipse with $n_{in} = 200$ is corrupted with the largest noise $\sigma_g = 9$. We use $M = 5000$ in the ellipse fitting experiments. In a test (Fig.6c) four ellipses are recovered

	red	*green*	*blue*	*cyan*
scale :	12.1	28.9	48.0	1321.2
inliers :	337	292	222	248
strength :	28.0	10.1	4.6	0.2.

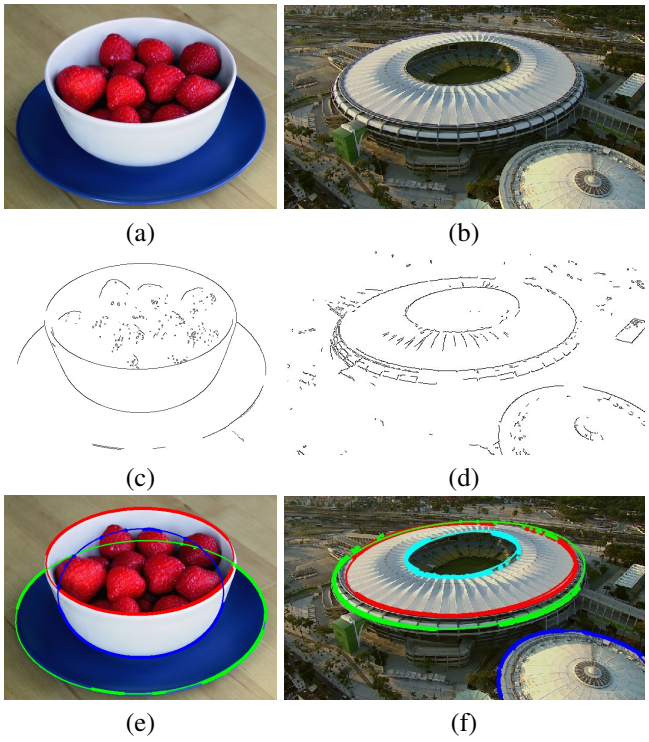

Fig. 7. 2D ellipses in real images. (a) Input image, *strawberries*. (b) Input image, *stadium*. (c) *Strawberries*: Canny edges, 4343 points. (d) *Stadium*: Canny edges, 4579 points. (e) *Strawberries*: Three strongest structures. (f) *Stadium*: Four strongest structures.

Based on strength, the first three structures are shown in Fig.6e.

The algorithm locates the correct three inlier structures 97 times from 100 tests. In the other three tests only the smallest ellipse is not estimated properly. The scales and the classified inliers with their standard deviations are

$$\begin{array}{rccc} scale: & 11.60 & 21.59 & 32.87 \\ & (1.54) & (3.64) & (14.71) \\ inliers: & 336.2 & 272.9 & 196.4 \\ & (8.2) & (27.5) & (53.2). \end{array}$$

The smallest ellipse is averaged from 97 tests only.

When the outlier amount reaches the limit, the inlier structure with weakest strength may no longer be returned before the outliers. The scale estimate becomes inaccurate due to the heavy outlier noise, and the outliers can form more dense structure with comparable strength. When 800 outliers (Fig.6b) are placed in the image, a test gives the result in Fig.6d. The outlier structure (blue) has a strength of 4.8, while the value of the inliers (cyan) is 3.9. The first two structures resist the noise due to stronger strengths.

In Fig.6f another case shows the limitation explained in Section 3.4. Two inlier structures interact with each other and the mean shift converges to incorrect modes.

The ellipse fitting was also tested with real images. In Fig.7a and Fig.7b two images containing several objects with elliptic shapes are shown. We obtain 4343 and 4579 points from Canny edge detection in Fig.7c and Fig.7d. With $M = 5000$, the strongest ellipses are drawn in Fig.7e and Fig.7f. From the data shown in Fig.7d, only the first two ellipses (red and green) are detected reliably in 98 tests out of 100, The blue and the cyan ellipses are much less stable due to the smaller amount of inliers. More stable results can be returned from preprocessed input data, where edge information is refined with local processing.

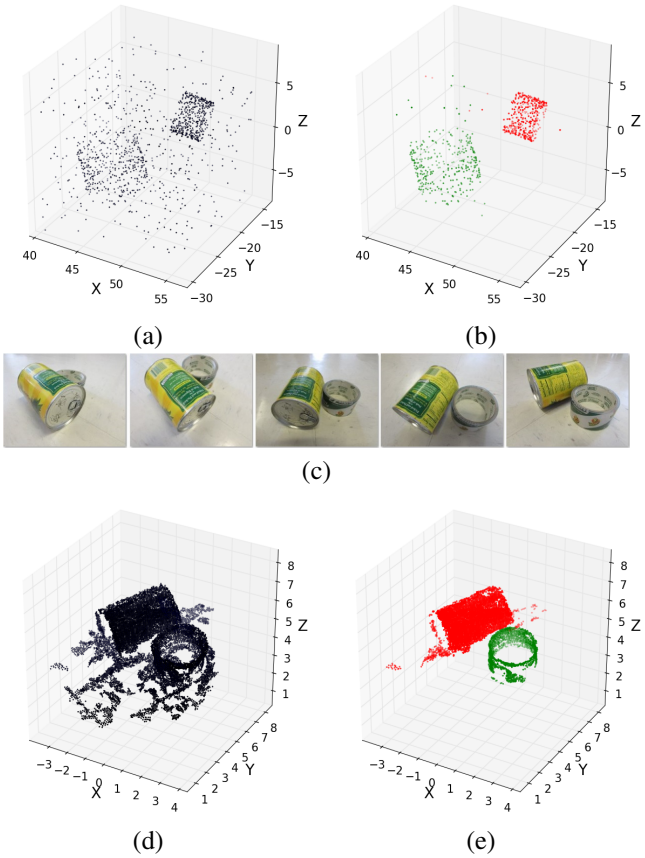

Fig. 8. 3D cylinder estimations. (a) Two synthetic cylinders and 500 outliers. (b) Recovered inlier structures. (c) Sample real images used for 3D reconstruction. (d) The 3D could of input points. (e) Recovered inlier structures.

4.3 3D Cylinder

The *3D cylinders* estimation has the noisy objective function

$$[\mathbf{y}_i \; 1] \, \mathbf{P} \, [\mathbf{y}_i \; 1]^\top \simeq 0 \qquad i = 1, \ldots, n_{in} \tag{24}$$

where $\mathbf{P}$ is a 4×4 symmetric matrix. The input variable $\mathbf{y} = [x \; y \; z]^\top$ gives the carrier $\mathbf{x} = [x^2 \; xy \; xz \; y^2 \; yz \; z^2 \; x \; y \; z]$. Although the quadric function introduces 9 degrees of freedom, a cylinder can be defined with only 5 points. Many different approaches to compute the cylinder were given in [2]. We start with the 9-points method and then apply the constraints for cylinder to the obtained quadric function. For a cylinder with no noise, the 3×3 leading principal submatrix of $\mathbf{P}$ is singular and has two identical eigenvalues. We set a small threshold to tolerate the noisy structure.

The transpose of the 9×3 Jacobian matrix is

$$\mathbf{J}^{\top}_{\mathbf{x}|\mathbf{y}} = \begin{bmatrix} 2x & y & z & 0 & 0 & 0 & 1 & 0 & 0 \\ 0 & x & 0 & 2y & z & 0 & 0 & 1 & 0 \\ 0 & 0 & x & 0 & y & 2z & 0 & 0 & 1 \end{bmatrix}. \quad (25)$$

In Fig.8a two cylinders are placed with 500 outliers. The inlier structures have radius $r = 2, 3$, the number of inliers $n_{in} = 400, 300$ and $\sigma_g = 0.1, 0.2$. The Gaussian noise is roughly 15% of the size of radius.

With $M = 2000$ three structures are returned.

	red	*green*	*outlier*
scale :	0.29	0.49	6.41
inliers :	413	340	447
strength :	1448.8	683.0	69.7.

Based on strength, the first two inlier structures are shown in Fig.8b.

The *VisualSFM* software [9], [30] is used to generate the point cloud of a 3D scene captured by an image sequence (Fig.8c). The point cloud consists of 12103 points (Fig.8d). Fig.8e shows the segmented cylinders, with 4062 points for the red and 1635 as green. The heights of the cylinders are not evaluated in these tests, which would require further post processing.

4.4 Fundamental matrix

The next experiment shows the estimation of *fundamental matrices*, with the linear relations introduced in Section 2.1. A recent paper [4], solved the non-convex problem of the rank-2 fundamental matrix iteratively by a convex moments based polynomial optimization. It compared the results with a few RANSAC type algorithms. The method required several parameters and each example contained only one single fundamental matrix.

When the motion between image pair involves only translation, the fundamental matrix is not enough for motion segmentation, as proved in [1]. Fig.9a and Fig.9b show that a large enough rotation is required to separate the objects. The fundamental matrix at the right of Fig.9a is incorrect since the points taken as one inlier structure cover both objects. In this case homography is the solution, as will be discussed again in Section 4.5.

The point correspondences used as the inputs are extracted by OpenCV SIFT with a distance ratio of 0.8, as suggested in [17]. Each of the first two examples Fig.10a and Fig.10b shows three rigid objects placed in different locations. The SIFT locates 457 and 614 matches, respectively. With $M = 5000$, the result of the first four inlier structures are

Fig.10a	*red*	*green*	*blue*	*cyan*
scale :	0.24	0.29	1.01	1.22
inliers :	136	89	86	53
strength :	565.8	302.4	85.4	43.4.

Fig.10b	*red*	*green*	*blue*	*cyan*
scale :	0.42	0.23	0.66	0.60
inliers :	185	76	196	43
strength :	442.6	328.2	297.2	72.0.

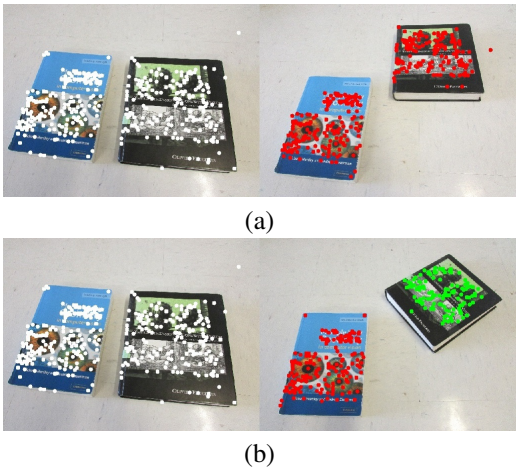

(a) (b)

Fig. 9. Motion segmentation using fundamental matrix. In all the subsequence images, the left image shown all the points, the right image only the inliers structures. (a) Translation transformation only. (b) Translation and rotation transformation.

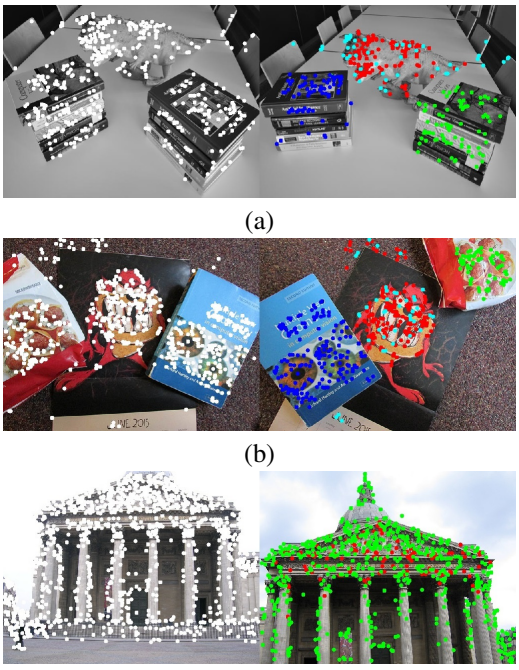

(a) (b) (c)

Fig. 10. Fundamental matrix estimation. (a) In the *dinabooks* from [21] three objects to be detected. (b) In the *books* three objects to be detected. (c) In the *Pantheon* one object to be detected.

The scales of the structures are small, therefore methods derived from RANSAC may also be used here.

As we discussed in Section 3.4, when the inlier points from a structure estimate only a small scale, it may not converge to the whole structure. In both Fig.10a and Fig.10b, a merge can be considered to combine the first (red) and the fourth (cyan) structures. The post-processing requires a threshold from the user, and should be done in the input space.

The SIFT matches are error-prone, false correspondences

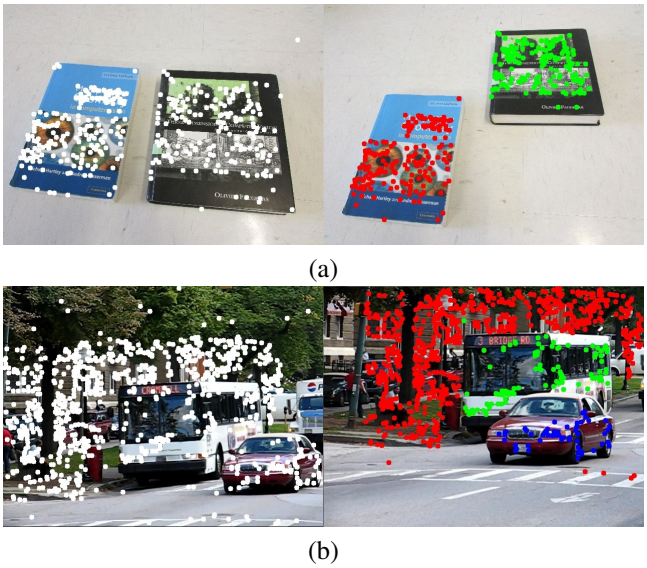

Fig. 11. Motion segmentation using homography when only translation exists. (a) Inliers in homography for Fig.9a. (b) Inliers of an image pair in *Hopkins 155 dataset*.

always exist and only by preprocessing we can reduce the incorrect matches. In Fig.10c we show an example containing 1327 matches while the final estimation gives an inlier structure with 308 points. The image on the right of Fig.10c shows the two structures after the estimation. The inlier scale is 1.39 (red), which is much smaller compared with the outliers at 191.4 (green).

If the images contain repetitive features, such as the exterior of buildings, parametrization of the repetitions can eliminate the uncertainty [24]. Since this involves preprocessing, is not detailed in the paper.

4.5 Homography

The final example is for 2D *homography* estimation. Each inlier structure is represented by a 3×3 matrix $\mathbf{H}$, which connects two planes inside the image pair

$$\mathbf{y}_i' \simeq \mathbf{H}\mathbf{y}_i, \quad i = 1, \ldots, n_{in} \tag{26}$$

where $\mathbf{y} = [x\ y\ 1]^\top$ and $\mathbf{y}' = [x'\ y'\ 1]^\top$ are the homogeneous coordinates in these two images.

As we mentioned in Section 2, the homography estimation has $\zeta = 2$. The input variables are $[x \quad y \quad x' \quad y']^\top$. Two linearized relations can be derived from the constraint (26) by the direct linear transformation (DLT)

$$\mathbf{A}_i\mathbf{h} = \begin{bmatrix} -\mathbf{y}_i^\top & \mathbf{0}_3^\top & x_i'\mathbf{y}_i^\top \\ \mathbf{0}_3^\top & -\mathbf{y}_i^\top & y_i'\mathbf{y}_i^\top \end{bmatrix} \begin{bmatrix} \mathbf{h}_1 \\ \mathbf{h}_2 \\ \mathbf{h}_3 \end{bmatrix} \simeq \mathbf{0}_2 \ . \tag{27}$$

The matrix $\mathbf{A}_i$ is 2×9 and both rows satisfy the relations with the vector derived from the matrix $\mathrm{vec}(\mathbf{H}^\top) = \mathbf{h} = \boldsymbol{\theta}$.

The carriers are obtained from the two rows of $\mathbf{A}_i$

$$\begin{aligned} \mathbf{x}^{[1]} &= [-x \ -y \ -1 \ 0 \ 0 \ 0 \ x'x \ x'y \ x']^\top \\ \mathbf{x}^{[2]} &= [0 \ 0 \ 0 \ -x \ -y \ -1 \ y'x \ y'y \ y']^\top. \end{aligned} \tag{28}$$

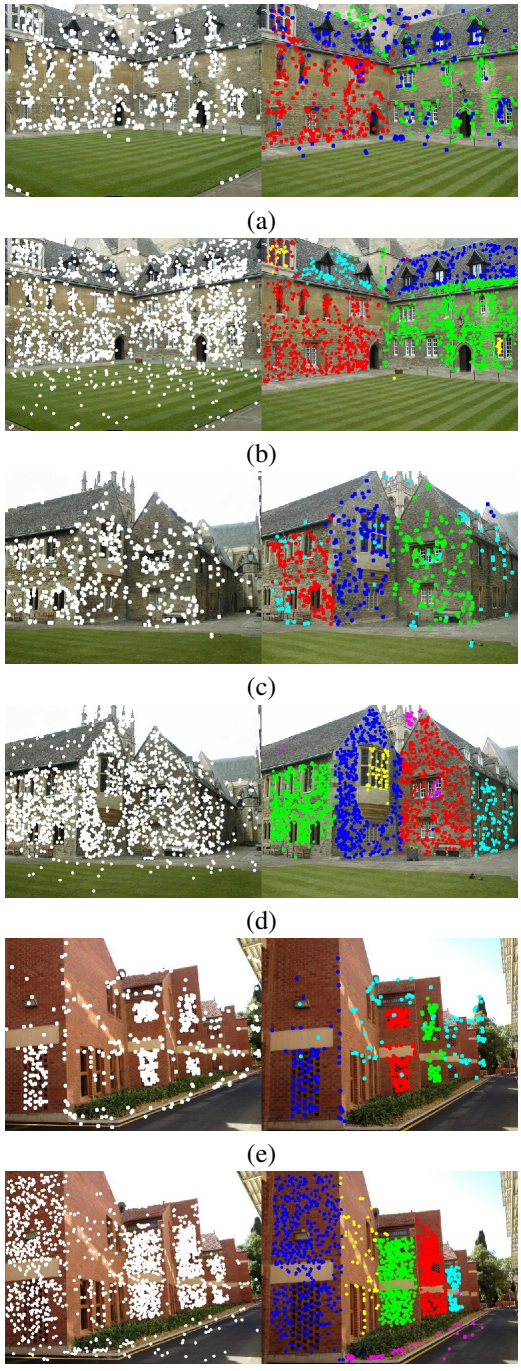

Fig. 12. Homography estimation. Comparison with [21]. (a), (c) and (e): Estimation results using OpenCV SIFT matches. (b), (d) and (f): Estimation results using the dataset from [21].

The transpose of the two 9×4 Jacobians matrices are

$$\mathbf{J}^{\top}_{\mathbf{x}_i^{[1]}|\mathbf{y}} = \begin{bmatrix} -\mathbf{I}_{2\times 2} & & x_i'\mathbf{I}_{2\times 2} & \mathbf{0}_2 \\ \mathbf{0}_2^{\top} & \mathbf{0}_{4\times 4} & \mathbf{y}_i^{\top} & \\ \mathbf{0}_2^{\top} & & \mathbf{0}_2^{\top} & 0 \end{bmatrix}$$
$$\mathbf{J}^{\top}_{\mathbf{x}_i^{[2]}|\mathbf{y}} = \begin{bmatrix} & -\mathbf{I}_{2\times 2} & & y_i'\mathbf{I}_{2\times 2} & \mathbf{0}_2 \\ \mathbf{0}_{4\times 3} & \mathbf{0}_2^{\top} & \mathbf{0}_4 & \mathbf{0}_2^{\top} & 0 \\ & \mathbf{0}_2^{\top} & & \mathbf{y}_i^{\top} & \end{bmatrix}. \quad (29)$$

Based on Section 2.2, for every $\boldsymbol{\theta}$ only the larger Mahalanobis distance is used for each input $\mathbf{y}_i,\ i = 1, \ldots, n$.

In Fig.11 the motion segmentation involving only translation is performed using homography. The same image pair as Fig.9a is properly segmented here, and another image pair from *Hopkins 155 dataset* also verifies the translational motion case. Note that the bus is stationary and the automobil is moving slightly. The planes in 2D are different than what the real objects would require in 3D, due to very small motion.

The outlier amount can affect the performance of any robust algorithms. For example, the paper [25] showed that the more traditional RANSAC type method, such as the PROSAC [5], failed in the homography estimation in the presence of many incorrect matches. Geometric and appearance priors were used to increase the amount of consistent matches before estimation. This type of preprocessing can also be applied before our algorithm.

In Fig.12 the significance of inlier amounts in the robust estimation is demonstrated. Each of the three groups has $M = 2000$ trials. In the table below we compare the inlier structures estimated from OpenCV SIFT data, Fig.12a,c,e, with those from the dataset used in [21] in Fig.12b,d,f. The results list the structures sorted by their strengths until the first outlier structure appears, denoted by an underbar. The number of input points (inlier/outlier) and the structures are

	red	green	blue	cyan	yellow	purple	INPUT
(a):	286	195	<u>213</u>				713
(b):	495	664	234	91	<u>37</u>		1940
(c):	131	161	145	<u>74</u>			536
(d):	474	512	529	124	54	<u>35</u>	1982
(e):	176	86	92	<u>109</u>			619
(f):	500	512	510	156	68	<u>40</u>	2084.

After testing the algorithm 100 times with the same input data, the results change only in the precise amount of inliers. It is clear that with more inlier points a better estimation can be returned. The data given by OpenCV SIFT usually return two-to-three stable structures, while the [21] dataset give four-to-five reliable results. This improvement can be achieved only by increasing the number of points in the inlier structures. As a result, reliable detection for more structures becomes possible due to the stronger strengths of inliers.

5 Discussion

A new robust algorithm is presented which does not require the scales specified by the users before the estimation, and can also handle different noise levels for multiple inlier structures in the presence of outliers. This method is easy to implement and can provide results in a few seconds (i7-2617M 1.5GHz), even for large-sized inputs such as the homography estimation.

In Section 5.1 we will summarize the conditions for robustness, and in Section 5.2 several open problems will be reviewed.

5.1 Conditions for robustness

We have discussed several limitations for the algorithm in Section 3.4 without considering the number of trials M for random sampling, which is the only parameter given by the user.

The RANSAC requires the inlier scale from the user, while the number of iterations is decided base on the expected inlier rate. This amount of sampling is usually valid when the inlier noise is relatively small. However, if the inliers are corrupted by larger noise, the model initialized by the sampling data set may not perfectly align with the true structure. The computation also becomes impractical in the case with low inlier rates, since the required number of iterations increases rapidly for a reliable result.

In the new algorithm M trials are used to estimate the scale. With the other robustness conditions satisfied, M has to be large enough for the weakest inlier structure. This process only gives an approximate scale estimate and a subset containing points mostly from a single structure. In the next step, the mean shift gains more efficiency for the structure estimation.

The required amount of M is much smaller than that in RANSAC, and relies strongly on the data to be processed. The complexity of the objective function, the size of the input data, the number of inlier structures, the inlier noise levels, and the amount of outliers can all affect the required number of trials. Without knowing the size of M, the user can run several tests with different M-s till the results become stable.

Once the interaction between inliers and outliers is apparent, the quality of the estimation cannot really be compensated by a larger M, since the initial set has become less reliable. Preprocessing of the input data is then required to reduce the number of outliers.

Three conditions can be given to improve the robustness of the multiple inlier structure estimation algorithm.

- Reduce the amount of outliers by preprocessing for a higher chance of correct output.
- Very large numbers of M are not necessary since these values will not improve the result.
- If an inlier structure comes out split, post processing in the input space is required to fuse them.

5.2 Open problems

We will list several open problems and discuss the possible solutions; however, further research and experiments are still needed.

Assume that the measurements of the input points have different covariances which are not specified. In many computer vision problems this situation is neglected but can still exist. The homoscedastic inlier covariances have the form

$$[\sigma_1^2 \ldots \sigma_{\mathbf{y}}^2]\mathbf{I}_{\mathbf{y}} = \begin{bmatrix} \sigma_1^2 & \cdots & 0 \\ \cdots & \cdots & \cdots \\ 0 & \cdots & \sigma_{\mathbf{y}}^2 \end{bmatrix} \quad (30)$$

with σ_j-s unknown. The computation for the covariance of the carrier (6) places the σ_j-s into the product of two Jacobian matrices.

A possible solution is to start with a uniform σ, that is, $\sigma^2\mathbf{I_y}$. Normally the algorithm should still work and several inlier structures will be returned. The number of inliers in each structure may not be the desired amount. Then for each inlier structure separately, apply the expansion process in the input space for each dimension to recover more inliers.

In face image clustering or projective motion factorization, there is only one carrier $\zeta = 1$ but an $m \times k$ matrix $\boldsymbol{\Theta}$ and a k-dimensional vector $\boldsymbol{\alpha}$ to be estimated. Since ζ is one dimensional, we use $\mathbf{x}$ instead of $\tilde{\mathbf{x}}$. The covariance $\sigma^2\mathbf{H}_i = \sigma^2\boldsymbol{\Theta}^\top\mathbf{C}_i\boldsymbol{\Theta}$, gives a $k \times k$ symmetric Mahalanobis distance matrix up to σ^2, for $i = 1, \ldots, n$

$$\mathbf{D}_i = \sqrt{\left(\mathbf{x}_i^\top\boldsymbol{\Theta} - \boldsymbol{\alpha}\right)^\top \mathbf{H}_i^{-1}\left(\mathbf{x}_i^\top\boldsymbol{\Theta} - \boldsymbol{\alpha}\right)} \tag{31}$$

expressed as the union of k vectors

$$\mathbf{D}_i = [\mathbf{d}_{i:1} \ \ldots \ \mathbf{d}_{i:k}]. \tag{32}$$

A possible solution is to order the Mahalanobis distances $\mathbf{d}_{[i:*]}$ for each column separately, and collect the inputs corresponding to the minimum sum of distances for $\epsilon\%$ of the data. The $k \times k$ matrices are reduced to k initial sets, one for each dimension.

Apply independently k times the expansion process described in Section 3.1 and define the $k \times k$ diagonal scale matrix

$$\mathbf{S}_k = \begin{bmatrix} \hat{\sigma}_1 & \cdots & 0 \\ \cdots & \cdots & \cdots \\ 0 & \cdots & \hat{\sigma}_k \end{bmatrix}. \tag{33}$$

The $k \times k$ covariance matrix $\mathbf{B}_i$ is computed as

$$\mathbf{B}_i = \mathbf{S}_k^\top\,\boldsymbol{\Theta}^\top\mathbf{C}_i\boldsymbol{\Theta}\,\mathbf{S}_k. \tag{34}$$

The structure estimation with mean shift is now multidimensional. Experiments will have to be performed to verify this solution.

If an image contains both lines and conics, there is no clear way to estimate them properly. See the examples in Fig.5 for trivial cases. Supposing we start with the lines, then some points from the conics may also be classified as lines. However, these points should be put back into the input data and used for the conics, otherwise some conics may not be detected. The same problem arises when we estimate the conics first. Only through supplemental processing may we separate the data of the lines from those of the conics.

The Python/C++ program for the robust estimation of multiple inlier structures is posted on our website at

coewww.rutgers.edu/riul/research/code/MULINL/index.html .

REFERENCES

[1] S. Basah, A. Bab-Hadiashar, and R. Hoseinnezhad, "Conditions for motion-background segmentation using fundamental matrix," *IET Comput. Vis.*, vol. 3, pp. 189–200, 2009.

[2] C. Beder and W. Förstner, "Direct solutions for computing cylinders from minimal sets of 3D points," in *ECCV2010*, volume 3952, Springer, pp. 135–146.

[3] H. Chen and P. Meer, "Robust regression with projection based M-estimators," in *ICCV2003*, pp. 878–885.

[4] Y. Cheng, J. A. Lopez, O. Camps, and M. Sznaier, "A convex optimization approach to robust fundamental matrix estimation," in *CVPR2015*, pp. 2170–2178.

[5] O. Chum and J. Matas, "Matching with PROSAC - Progressive sample consensus," in *CVPR2005*, volume I, pp. 220–226.

[6] D. Comaniciu and P. Meer, "Mean shift: A robust approach toward feature space analysis," *IEEE Trans. Pattern Anal. Mach. Intel.*, vol. 24, pp. 603–619, 2002.

[7] E. Elhamifar and R. Vidal, "Sparse subspace clustering: Algorithm, theory, and applications," *IEEE Trans. Pattern Anal. Mach. Intel.*, vol. 35, pp. 2765–2781, 2013.

[8] M. A. Fischler and R. C. Bolles, "Random sample consensus: A paradigm for model fitting with applications to image analysis and automated cartography," *Comm. Assoc. Comp. Mach*, vol. 24, pp. 381–395, 1981.

[9] Y. Furukawa and J. Ponce, "Accurate, dense, and robust multiview stereopsis," *IEEE Trans. Pattern Anal. Mach. Intel.*, vol. 32, pp. 1362–1376, 2010.

[10] R. I. Hartley and A. Zisserman, *Multiple View Geometry in Computer Vision*. Cambridge University Press, second edition, 2004.

[11] T. Hassner, L. Assif, and L. Wolf, "When standard RANSAC is not enough: Cross-media visual matching with hypothesis relevancy," *Machine Vision and Applications*, vol. 25, pp. 971–983, 2014.

[12] G. B. Hughes and M. Chraibi, "Calculating ellipse overlap areas," *Comput. Visual Sci.*, vol. 15, pp. 291–301, 2012.

[13] H. Isack and Y. Boykov, "Energy-based geometric multi-model fitting," *International J. of Computer Vision*, vol. 97, pp. 123–147, 2012.

[14] K. Kanatani, "Ellipse fitting with hyperaccuracy," *IEICE Trans. Inf. & Syst.*, vol. E89-D, pp. 2653–2660, 2006.

[15] I. Lavva, E. Hameiri, and I. Shimshoni, "Robust methods for geometric primitive recovery and estimation from range images," *IEEE Trans. Sys. Man and Cybernetics B*, vol. 38, pp. 826–845, 2008.

[16] R. Litman, S. Korman, A. Bronstein, and S. Avidan, "Inverting RANSAC: Global model detection via inlier rate estimation," in *CVPR2015*, pp. 5243–5251.

[17] D. G. Lowe, "Distinctive image features from scale-invariant keypoints," *International J. of Computer Vision*, vol. 60, pp. 91–110, 2004.

[18] S. Mittal, S. Anand, and P. Meer, "Generalized projection-based M-estimator," *IEEE Trans. Pattern Anal. Mach. Intel.*, vol. 34, pp. 2351–2364, 2012.

[19] S. Mittal and P. Meer, "Conjugate gradient on Grassmann manifolds for robust subspace estimation," *Image and Vision Comp.*, vol. 30, pp. 417–427, 2012.

[20] L. Moisan, P. Moulon, and P. Monasse, "Automatic homographic registration of a pair of images, with a contrario elimination of outliers," *Image Proc. Online*, vol. 2, pp. 56–73, 2012.

[21] T. T. Pham, T.-J. Chin, J. Yu, and D. Suter, "The random cluster model for robust geometric fitting," *IEEE Trans. Pattern Anal. Mach. Intel.*, vol. 36, pp. 1658–1671, 2014.

[22] R. Raguram, O. Chum, M. Pollefeys, J. Matas, and J. Frahm, "USAC: A universal framework for random sample consensus," *IEEE Trans. Pattern Anal. Mach. Intel.*, vol. 35, pp. 2022–2038, 2013.

[23] R. Raguram, J.-M. Frahm, and M. Pollefeys, "A comparative analysis of RANSAC techniques leading to adaptive real-time random sample consensus," in *ECCV2008*, volume 5303, Springer, pp. 500–513.

[24] F. Schaffalitzky and A. Zisserman, "Geometric grouping of repeated elements within images," in *Shape, Contour and Grouping in Computer Vision*, Springer, 1999, pp. 165–181.

[25] E. Serradell, M. Özuysal, V. Lepetit, P. Fua, and F. Moreno-

Noguer, "Combining geometric and appearance priors for robust homography estimation," in *ECCV2010*, volume 6313, Springer, pp. 58–72.

[26] Z. L. Szpak, W. Chojnacki, and A. van den Hengel, "Guaranteed ellipse fitting with a confidence region and an uncertainty measure for centre, axes, and orientation," *J. Math. Imaging Vision*, vol. 52, pp. 173–199, 2015.

[27] R. B. Tennakoon, A. Bab-Hadiashar, Z. Cao, R. Hoseinnezhad, and D. Suter, "Robust model fitting using higher than minimal subset sampling," *IEEE Trans. Pattern Anal. Mach. Intel.*, vol. 38, pp. 350–362, 2016.

[28] A. Vedaldi, H. Jin, P. Favaro, and S. Soatto, "KALMANSAC: Robust filtering by consensus," in *ICCV2005*, volume 1, pp. 633–640.

[29] H. Wang, T.-J. Chin, and D. Suter, "Simultaneously fitting and segmenting multiple-structure data with outliers," *IEEE Trans. Pattern Anal. Mach. Intel.*, vol. 34, pp. 1177–1192, 2012.

[30] C. Wu, "Towards linear-time incremental structure from motion," in *Inter. Conf. of 3D Vision*, 2013, pp. 127–134.